Support effects of NiW hydrodesulfurization catalysts from experiments and DFT calculations

J.N. Díaz de León[a,*], J. Antunes-García[a], G. Alonso-Nuñez[a], T.A. Zepeda[a], D.H. Galvan[a], J.A. de los Reyes[b], S. Fuentes[a]

[a] *Universidad Nacional Autónoma de México, Centro de Nanociencias y Nanotecnología, Km. 107 carretera Tijuana-Ensenada, C.P. 22800, Ensenada, Baja California, Mexico*
[b] *Departamento de Ciencias Básicas e Ingeniería, UAM-Iztapalapa, San Rafael Atlixco 186, Col. Vicentina, Iztapalapa, México, D. F. 09340, Mexico*

A B S T R A C T

The present work deals with the effect of common carriers and binary mixed oxide materials in the preparation of oxide and sulfidic NiW catalysts. Experimental characterization and DFT theoretical study of the intrinsic support interaction of WS_2 and $Ni-WS_2$ clusters revealed that each oxide conferred to the NiW catalysts different activity, dispersion, promotion, total acidity and specific surface bonding. Initially, we present the binding energy obtained by routine UV–vis DRS of WOx polymeric species over the different supports as indicator of the dispersion by obtaining the next nearest neighbors (N_W). These N_W values seem to correlate well with the WS_2 slab length reported in our previous work. The XPS results pointed to a better promotion of the active phase when catalysts were prepared over Al_2O_3-TiO_2 and ZrO_2-TiO_2 mixed oxides. Besides, a correlation was confirmed between the total acidity observed by FTIR of adsorbed pyridine and the hydrodesulfurization of the DBT diesel model molecule. Additionally, DFT theoretical calculations revealed that the promoted cluster tends to be bent by the interaction with the support. This bending of the promoted WS_2 slabs was observed experimentally in our materials, especially in the three more active NiW catalysts.

1. Introduction

One of the greatest industrial challenges to contend with environmental pollution is the reduction of sulfur contents in gasoline and diesel fuels to ever lower levels. Around the globe, the sulfur content limits are about 10–50 ppm in gasoline and diesel. Furthermore, these sulfur levels are expected to be reduced to 10 ppm, and the "zero sulfur horizon" is coming soon [1]. To face these demanding environmental standards, the development of more active hydrodesulfurization (HDS) catalysts looks like to be the most promising way to improve fuel quality without negative impact on capital investment (compatibility of the HDS catalysts with the current HDS refining units) [2]. In industrial processes, the hydrotreating catalysts are composed of molybdenum sulfide phase "MoS_2" promoted by cobalt or nickel and usually supported on gamma alumina (γ-Al_2O_3) [3]. The use of γ-Al_2O_3 as support is ascribed to its mechanical properties, to a relatively low cost and to its ability to provide high dispersion of the active phases [3–5]. Improvements in the preparation of this oxide as well as the use of additives such as fluorine and phosphate led to the last generation of commercialized hydrotreating catalysts [6]. At the same time, many

different approaches to preparing better catalysts have been tested [6–8]. Especially, it is well known that the catalytic activity of HDS catalysts may be increased by changing the nature of the support [9]. In this sense, many reports exhibit clear differences in the formation of the sulfided active phases, particularly in the morphology, the dispersion and in the sulfurability depending on the chosen support. Studies using SiO_2, TiO_2, ZrO_2 and Al_2O_3 [6,7,10,11] as support have shown that the term "support effect" involves several aspects such as modification of electronic properties, improvements of the morphological and textural properties and even increase of the surface acid sites [11]. Other "unusual" supports have also been studied, *i.e.* amorphous silica-alumina (ASA) [12], carbon-coated alumina [13], Ti-MCM-41 [14], KIT-6 [15] and mixed oxides such as Al_2O_3-TiO_2 [16,17], ZrO_2-TiO_2 [18], MgO-TiO_2 [19], MgO-Al_2O_3 [20], γ-Al_2O_3, α-Ga_2O_3 [21] and even ZrO_2–TiO_2–Al_2O_3 ternary mixed oxide [22,23]. Some of these materials, when used as supports, may produce four to five-fold higher activity of Mo and W-based systems [2]. However, the vast majority of research on HDS catalysts has been done concerning the CoMo and NiMo systems, and the acquired knowledge was extended to the NiW system by similarity. Therefore, direct information of the NiW system is

---

scarcely found despite the fact that the NiW catalyst has shown different catalytic behavior such as [21] different selectivity, yield, and better poisoning resistance against nitrogenated compounds than the typical CoMo and NiMo systems. We recently published that an appropriate selection of the support can dramatically increase the catalytic performance [24]. Thus, NiW/ Al$_2$O$_3$-TiO$_2$ (AT) and NiW/ZrO$_2$-TiO$_2$ (ZT) exhibited the highest 3-methyl thiophene hydrodesulfurization activity among a series of supported NiW catalysts. The micrographs by high-resolution transmission microscopy (HRTEM) analysis exhibited a clear variation of the morphology of the sulfided active phase depending on the support. In this work, we intend to obtain further insight on the support effect for W and NiW-based catalysts. Typical single oxides such as γ-Al$_2$O$_3$ (A), SiO$_2$ (**S**), TiO$_2$ (T) and ZrO$_2$ (Z) as well as the aforementioned AT and ZT mixed oxides were synthesized by a sol-gel methodology and calcined at 500 °C. The W and NiW catalysts were prepared by a pore-filling method with a surface density of 2.8 W atoms per square nanometer (W nm^{-2}) keeping constant the Ni/(Ni + W) atomic ratio at 0.41. Catalysts in the oxide state were characterized by X-ray diffraction (XRD), ultraviolet-visible spectroscopy (UV–vis), and inductively coupled plasma (ICP). The catalytic activity of the sulfided NiW catalysts was evaluated in a gas phase continuous flow microreactor operating at high hydrogen pressure (490 psi) with dibenzothiophene (DBT) as a diesel model molecule. Finally, sulfided materials were characterized by FTIR of adsorbed pyridine and X-ray photoelectron spectroscopy (XPS). Additionally, the development of the computational calculations by integration of density functional theory (DFT) demonstrated that they could help in understanding the behavior of sulfide phases [25]. Therefore, DFT simulations were carried out to further analyze the interactions between the WS$_2$ and NiWS clusters with the supports.

2. Experimental section

2.1. Preparation of supports

The A, T, Z, **S**, AT and ZT supports were synthesized by the sol-gel method. The entire sol-gel synthesis procedure was reported previously in [24]. Typically, pure γ-Al$_2$O$_3$ (A), SiO$_2$ (S), TiO$_2$ (T), ZrO$_2$ (Z) and mixed Al$_2$O$_3$-TiO$_2$ (AT) and ZrO$_2$-TiO$_2$ (ZT) supports were synthesized by sol-gel method. The sol-gel method was as follows: 10 mL of metal oxide precursor was dissolved in 166 mL of 2-propanol (Aldrich 98%) under continuous stirring for 2 h at 0 °C. Subsequently, the hydrolysis solution (a mixture of 11.5 mL H$_2$O and 0.57 mL HNO$_3$ 70%) was added dropwise to the previous solution. The sol was left at 0 °C for 24 h to form the gel and was then placed into a crystallizer at 70 °C for 48 h to eliminate the solvent. The obtained solids were calcined at 500 °C for 4 h at a heating rate of 1 °C min^{-1}. The AT mixed oxide was prepared with an atomic ratio (Al/Ti) = 2; for the ZT material the atomic ratio (Zr/Ti) was fixed at 1. In the case of the SiO$_2$ (S) material, 1 g of P123 (MW 5800, Aldrich) was dispersed in an HCl solution (0.1 g, 2 M) and H$_2$O (0.9 g) in EtOH (10 g). After 2 h of stirring, TEOS (2.08 g, 10 mMol) was added. The solution was aged for 24 h and then dried at 120 °C. Finally, the white solid was calcined at 500 °C for 4 h with a heating rate of 1 °C min^{-1}.

2.2. Preparation of catalysts

In a typical preparation of the W/(x) catalyst (where x is any of the supports above), the corresponding support was impregnated with a solution of ammonium metatungstate (AMT), (NH$_4$)$_6$W$_{12}$O$_{39}$·xH$_2$O (, Aldrich Chemical, 99.99%) by using the pore filling method. After 12 h of maturation, the obtained solid was dried at 120 °C for 12 h and calcined at 450 °C for 4 h under air-stream (5.16 × 10^{-3} mol min^{-1}) with a heating rate of 1 °C min^{-1}. For NiW/(x) catalysts, the solution of AMT was first impregnated on the support, left for 12 h, and then dried under an air stream at 125 °C for 12 h, with a heating rate of 1 °C min^{-1}.

Then Ni was impregnated under the same conditions, and the final green solid was calcined on the same terms. The concentration of the AMT solution was selected to obtain 2.8 W atoms nm^{-2} (pH ≈ 3.7) while nickel was adjusted to define a nominal atomic ratio r = (Ni/(Ni + W)) equal to 0.41 (pH ≈ 4.4). After calcination, all materials were sieved at 80–100 mesh (0.15-0.18 mm). BET surface areas were 320, 55, 78, 343, 428 and 332 m2 g-1 for A, T, Z, **S**, AT and ZT supports, respectively. Full textural properties for the supports were provided in our previous work [24]. The Ni and W elemental weight % (wt.-%) contents in each catalyst were measured by ICP.

2.3. UV–vis diffuse reflectance spectroscopy

The evolution of the absorption edge energy of the oxide state catalysts was studied by UV–vis spectroscopy using an AVANTES Avaspec 2048 UV–vis spectrophotometer equipped with an AvaLight-DHS light source. The absorption edge energies were obtained according to the Kubelka-Munk function as described by Barton [26].

2.4. In-situ sulfidation

The catalysts were activated by *in-situ* sulfidation in the reactor as follows: firstly, the sample was flushed with nitrogen flow and the temperature was gradually increased to 150 °C. Then, the stream was switched to the sulfidation mixture (H$_2$/H$_2$S 15% v/v H$_2$S) with a flow of 40 mL·min^{-1}, and the temperature then increased to 400 °C with a heating rate of 5 °C min^{-1}. The sulfidation continued under these conditions for 4 h. Then the sample was cooled to room temperature, changing the sulfidation flow to the reaction mixture when the temperature reached 150 °C.

2.5. Catalytic activity measurements

The HDS of DBT was evaluated under high-pressure (490 psi) in a biphasic continuous microflow reactor. The saturator with DBT was heated to 170 °C, and then a H$_2$ flow of 200–400 cm^3 min^{-1} was sent in through the reactor. After this step, the flow was sent to a condensation system operating at 140 °C to stabilize the saturation point at this temperature, reaching a DBT concentration of 3.03 × 10^{-6} mol L^{-1} (1.51 × 10^{-3} psi). The reaction was tested at 260 °C, and the flow was controlled to avoid a high conversion. The catalyst weight was 50 mg of the pre-activated catalyst. The products were analyzed by gas chromatography with a flame ionization detector (FID), while the rates were estimated at differential reactor conditions at a low conversion (x < 20%) considering steady state conditions (after 12 h on stream). Under steady state conditions we considered at least 10 stabilized samples to obtain an average conversion ($\bar{x}$) value. The $\bar{x}$ where obtained as follows:

$$\bar{x} = \frac{C^0_{DBT} - C^{260°C}_{DBT}}{C^0_{DBT}} \qquad (1)$$

where C^0_{DBT} is the initial concentration at 140 °C and $C^{260°C}_{DBT}$ is the concentration after reaction at 260 °C.

Finally, the reaction rates were obtained with

$$-r_{DBT} = \frac{\bar{x} * Q^0_{DBT}}{m_{cat}} \qquad (2)$$

where Q^0_{DBT} is the molar flow of DBT and m_{cat} is the sulfided catalyst mass used in the specific catalytic test.

2.6. FTIR of adsorbed pyridine on the sulfided catalysts

The FTIR studies of adsorbed pyridine were recorded on an Agilent 660 FTIR spectrophotometer at a resolution of 4 cm^{-1} with a specially designed Praying Mantis diffuse reflection attachment and low-

temperature cell (Harrick) for *in-situ* measurements. The samples were sulfided *ex-situ* with a 15% H_2/N_2 mixture at 623 K for 2 h and then degassed under 10^{-5} mbar for 1 h. Afterwards, they were cooled to room temperature before being exposed to pyridine. Pyridine adsorption was performed at 373 K and 5 mbar for 30 min. The IR spectra were recorded after evacuation (10^{-5} Torr) of physically adsorbed pyridine at 393 K for 0.5 h.

2.7. X-ray photoelectron spectroscopy of sulfided catalysts

The XPS spectra of the samples were recorded using a SPECS® spectrometer with a PHOIBOS® 150 WAL hemispherical energy analyzer with angular resolution (< 0.5 degrees), equipped with an XR 50 Al-X-ray and µ-FOCUS 500 X-ray monochromator (Al excitation line) sources. To protect the fresh and spent samples from air contact, they were kept under argon atmosphere before being transferred into a mobile XPS chamber and finally to the XPS apparatus. Samples were first degassed at 10^{-5} mbar in the pretreatment chamber before being transferred to the analysis chamber, where residual pressure was kept below 7×10^{-9} mbar during data acquisition. The binding energies (B_E) were referenced to the C 1 s peak (284.8 eV) to account for the charging effects. Mixed Gaussian/Lorentzian functions were employed to fit the spectrum after background subtraction according to the Shirley equation. Surface atomic ratios were calculated from the peak area ratios normalized by the corresponding atomic sensitivity factors provided by the software.

2.8. Computational details

The different supports were modeled by DFT calculations, considering the crystalline structure and the surface plane of each single or mixed oxide. The data used to optimize these supports are described in Table 1. For the pure supports A, T, Z and *S* the corresponding metal and the oxygen atoms considered were the (100), (010), (001) and (001) surface planes, respectively. The mixed AT and ZT supports were labeled with a superscript (I, II or III), corresponding to solid solutions in three different configurations. The configuration I considered the Al or Zr atoms on top of the surface for samples AT and ZT, respectively. The configuration II considered the Ti atoms on top of the surface for both solid solutions. The configuration III considered that both Al and Ti atoms and both Zr and Ti atoms were on the top of the surface for the AT and ZT simulations respectively. The case used for the computational calculations are shown in Fig. 1. The optimized cluster-support

Table 1
Details of the supports considered for DFT calculations.

Support	Symbology	Surface plane	Crystallinity and atoms exposed
γ-Al_2O_3	A	(100)	γ-Al_2O_3 with Al atoms on the surface
Al_2O_3-TiO_2-I	AT^I	(100)	Mixed AlTi oxide with Al atoms on the surface
Al_2O_3-TiO_2-II	AT^{II}	(200)	Mixed AlTi oxide with Ti atoms on the surface
Al_2O_3-TiO_2-III	AT^{III}	(111)	Mixed AlTi oxide with both Al and Ti atoms on the surface
TiO_2	T	(010)	Anatase structure with Ti on the surface
SiO_2	*S*	(001)	Stishovite structure with Si on surface
SiO_2	*S*^{II}	(001)	Cristobalite structure with Si on the surface
ZrO_2	Z	(001)	Monoclinic ZrO_2 structure with Zr on the surface
ZrO_2-TiO_2-I	ZT^I	(100)	Mixed ZrTi oxide with Zr atoms on the surface
ZrO_2-TiO_2-II	ZT^{II}	(200)	Mixed ZrTi oxide with Ti atoms on the surface
ZrO_2-TiO_2-III	ZT^{III}	(011)	Mixed ZrTi oxide with both Zr and Ti atoms on the surface

configurations were obtained by density functional theory calculations (DFT) with the QUANTUM-ESPRESSO code [27], which uses pseudopotentials and a plane wave basis set. The exchange-correlation potential was approximated by the generalized gradient approximation (GGA) using the Perdew-Burke-Ernzenhof (PBE) functional [28,29]. The atomic positions of cluster/support bulk unit cells, and cluster/support configurations, were fully relaxed until the energy convergence criteria of $\sim 5 \times 10^{-5}$ eV were reached.

On the other hand, the adsorption energy E_{ads} for clusters on different surfaces was calculated as follows:

$$E_{ads} = E_{(cluster+support)} - E_{support} - E_{cluster} \qquad (3)$$

where $E_{(cluster+support)}$ refers to the energy of the configuration formed by the adsorption of the corresponding cluster to the substrates, $E_{support}$ and $E_{cluster}$ refer to the configurational energy of the bare support and plain cluster, respectively. We defined that the negative values of E_{ads} indicate an exothermic process.

3. Results

3.1. Characterization of supports

3.1.1. UV–vis diffuse reflectance spectroscopy

Fig. 2 presents the DRS spectra of the calcined supports. As expected, the silica sample (S) does not present signals of energy absorption because pure siliceous materials such as SBA or MCM do not exhibit energy absorptions in this range (200–800 nm) [30]. All other samples exhibited absorption bands, related to ligand-metal charge transfer (LMCT) transitions. The alumina sample (A) revealed only a weak absorption arising near 250 nm, in agreement with the strong insulating character of γ-alumina [31]. This band corresponds to the LMCT transitions from O^{2-} to Al^{3+} [32]. For the Z sample, an absorption edge beginning near 280 nm with a maximum at 220 nm was observed, which is associated with an O^{2-} to Zr^{4+} transition. The pure zirconia sample showed two absorption shoulders, the first one clearly located in a region between 200 and 250 nm, and the second one as an absorption tail from 250 to 400 nm [31]. These differences are probably due to the preferred monoclinic phase composition, as XRD previously showed. The titania sample displayed at least 3 absorption shoulders, the first one between 200–280 nm, the second one from 280 to 320 nm and the last one from 320 to 430 nm. The first absorption band (200,280 nm) was attributed to the transition between the O^{2-} ligand and the isolated Ti^{4+} in tetrahedral coordination [33]. The second region at 280–320 nm was attributed to the presence of Ti ions in pentahedral and octahedral coordinations [34]. The third absorption band in the range of 320–430 nm was related to the $O^{2-} \rightarrow Ti^{4+}$ transition, characteristic of TiO_2 anatase. Furthermore, this region could be linked to the Ti^{4+} octahedral coordination. In the spectra obtained from ZT and AT mixed materials, two absorption bands were detected. One band located at 200–280 nm and the other one with an edge near 400 nm. Both spectra resembled the T sample spectrum closely indicating that $O^{2-} \rightarrow Ti^{4+}$ transitions were predominant in these samples. However, both spectra showed a shift toward shorter wavelengths. This similarity was related to the titanium oxide in more insulating oxides dilution (Al_2O_3 and ZrO_2 as seen), causing increases in the energy gap [31]. Ramirez et al. [35] reported similar electronic spectra for the mixed Al_2O_3-TiO_2 supports.

According to a previous report [36], the absorption edge energy represents the optical band gap energy of an insulator (or semiconductor), therefore, the absorption edge energies (E_b) for calcined samples were obtained by plotting $[F(R \infty) \cdot \hbar\nu]^2$ *vs.* $\hbar\nu$, as shown in the inset of Fig. 2. The E_b values were as follows: 5.62, 4.98, 3.37, 3.33 and 3.01 eV for A, Z, ZT, AT and T samples, respectively. None E_b value was obtained for the *S* sample. Table 2 summarizes the obtained E_b values compared with previously reported E_b values [31,37]. Values for Z and T samples agreed with those previously reported (see Table 2).
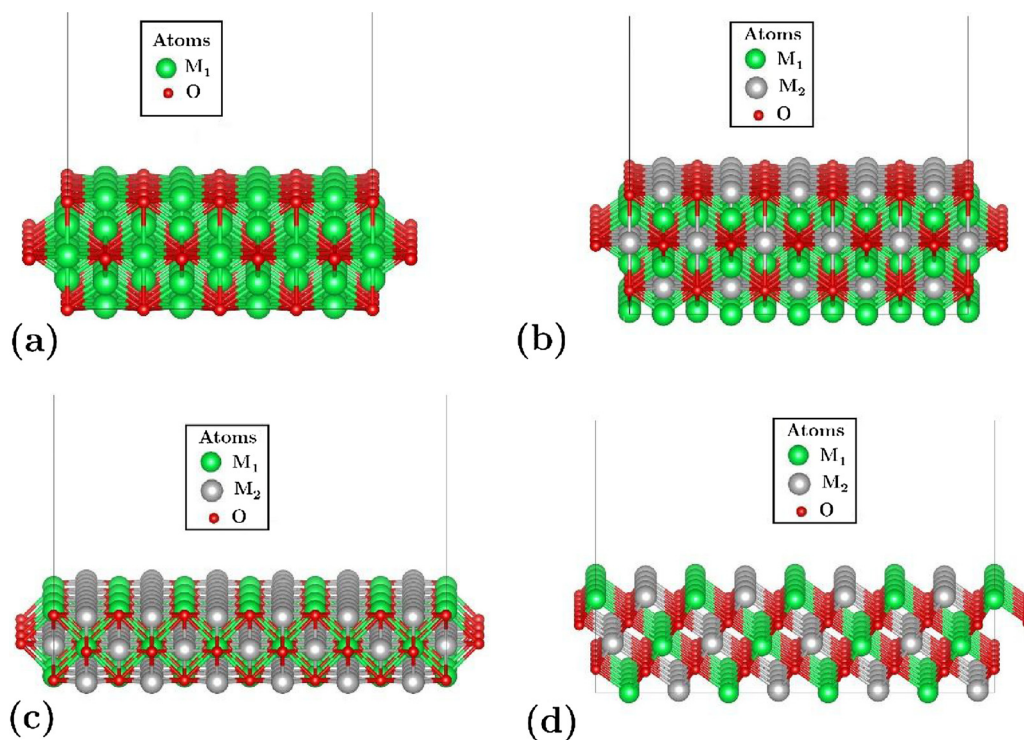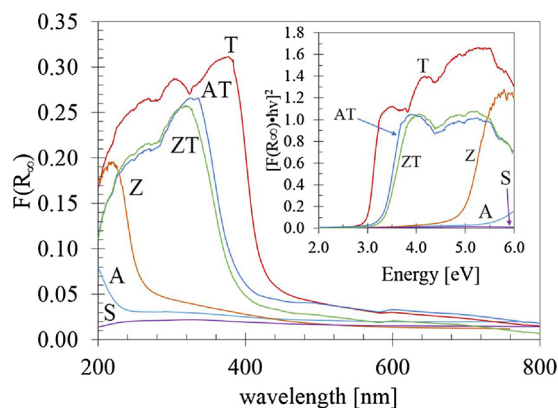
Fig. 2. UV–vis diffuse reflectance absorption spectra of samples A, T, Z, **S**, AT and ZT. Absorption edge energies were determined by the intercept of a linear fit to the absorption edge (Tauc plot as inset).

Table 2
Band-gap energy data for the supports after calcination at 500 °C.

E_b [eV]	A	T	Z	S	ZT	AT
Literature values	5.1[c], 7.0-7.6[b]	3.0[b], 3.22[a]	5.0[a], 5.2[b]	–	~3.31[a]	–
Our experimental values	5.5	3.0	5.0	–	3.4	3.3

[a] Data from reference [37].
[b] Data from reference [31].
[c] Data from reference [39].

However, the A sample showed a far shift of 1.7 eV from its typical values (7–7.6 eV). This value for alumina can be associated to the specific synthesis method used and to the Al_2O_3 crystalline form [38]. The data obtained for the ZT and AT mixed oxides were very similar to each other, but slightly higher than the value for the T sample. In conclusion, the presence of Al_2O_3 and ZrO_2 in mixed oxides with TiO_2 increases the band gap and slightly decreases the semiconducting

character of these samples.

3.2. Characterization of W and NiW-based catalysts

3.2.1. Composition of catalysts

The elemental analyses of all prepared catalysts are presented in Table 3. The impregnation density of 2.8 W at. nm^2 was the same for all materials; this value resulted in an average of 21 ± 2.1 wt.% of W for NiW/A, NiW/S, NiW/AT and NiW/ZT. In the case of the low area supports T and Z, the corresponding catalysts showed 4.8 ± 0.4 wt.% of W. At the same time, this impregnation density had an impact on the quantity of impregnated Ni. As the relation of Ni and W was settled to 0.41, this ratio produced catalysts with around 4 wt.-% of Ni for NiW/A, NiW/S, NiW/AT and NiW/ZT and 1% for the NiW/T and NiW/Z samples. Indeed, the Ni/(Ni + W) ratio remained around 0.39 ± 0.2, which is considered in the range of optimum specific catalytic activity [40].

3.2.2. UV–vis DRS for the WO_x catalysts

DRS spectra of various tungsten-containing commercial reagents were obtained, such as crystalline WO_3 and sodium tungstate ((Na_2WO_4)-H_2O), to be used as standard W compounds (Aldrich Chemical 99.99%). As the method indicated, samples were chosen with a wide range of WO_x domain size, well-known coordination symmetry and absorption edge energy [37]. Sodium tungstate ((Na_2WO_4)-H_2O) presents a W^{6+} coordinated tetrahedral geometry of four oxygens. Typically, this kind of centers are isolated with zero degrees of local aggregation. Thus, its average number of W next nearest neighbors (N_W) is almost zero; this is the reason why it exhibits an absorption edge energy as high as 4.89 eV [36]. In the case of tungsten trioxide (WO_3), it displays a W^{6+} coordinated octahedral geometry of six oxygens in the middle of a three-dimensional crystalline network, which means six W nearest neighbors. Therefore, an absorption edge energy as low as 2.59 eV has been reported. Barton et al. described that ammonium metatungstate ((NH_4)$_6$$H_2$$W_{12}$$O_{40}$*$6H_2O$) (AMT) contains octahedral WO_6 with four WO_6 neighbors and an absorption edge energy of ca. 3.23 eV [37]. Meanwhile, Valigi et al. reported 5.4, 2.85 and 3.45 eV for the E_b values corresponding to ((Na_2WO_4)-H_2O), WO_3 and AMT,

Table 3
Nominal and elemental composition for all supported W and NiW catalysts.

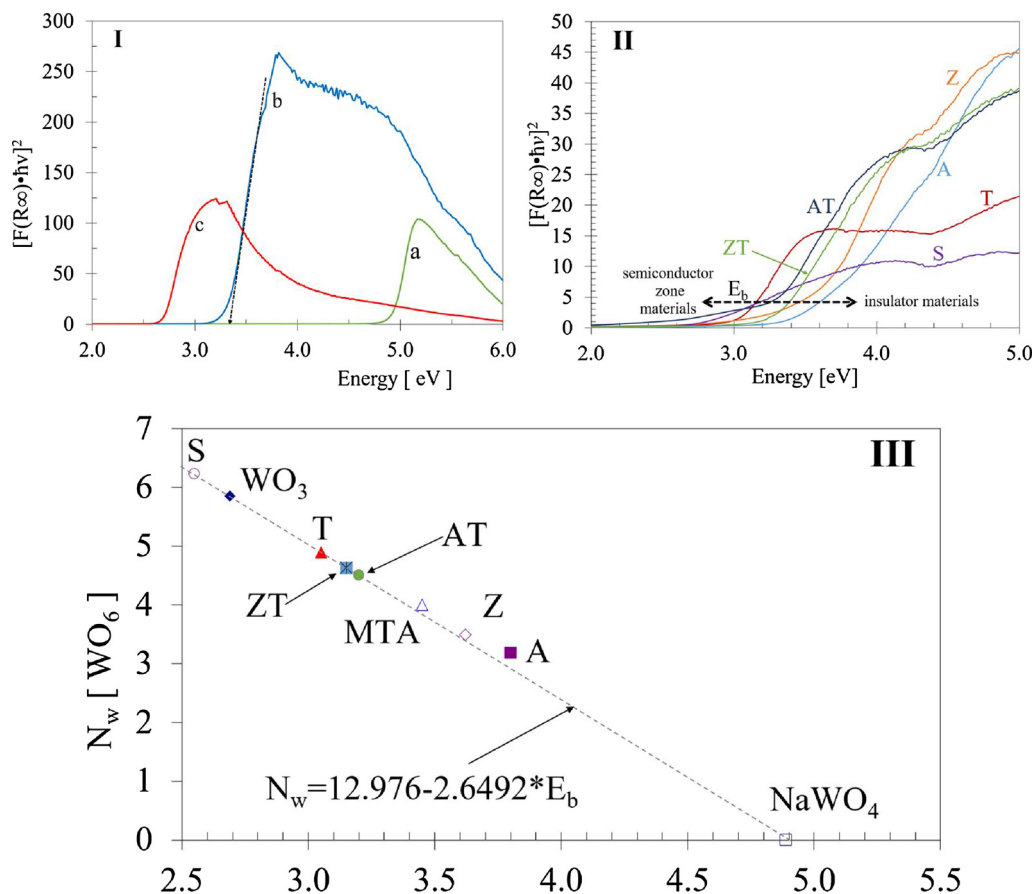| Sample	Nominal composition				ICP analysis			
	W	Ni	W	Ni	W/supp	NiW/supp		
	at. nm^{-2}	Ni/(Ni + W)	%wt.W	%wt.Ni	%wt.W	%wt.W	%wt.Ni	Ni/(Ni + W)
commercial	–	0.38	20.0	4.0	–	–	–	–
A	2.8	0.41	19.2	4.3	19.3	18.9	4.0	0.40
T			4.4	1.0	4.1	4.0	0.9	0.40
Z			6.0	1.3	5.2	5.0	1.0	0.41
S			20.2	4.5	20.0	19.8	3.8	0.38
AT			23.4	5.2	22.5	22.1	4.2	0.37
ZT			19.7	4.4	18.9	18.6	3.9	0.40

Fig. 3. I) UV–vis DRS reference materials, spectral energy transformation, a) NaWO$_4$, b) AMT, c) WO$_3$. II) Tauc plot of the UV–vis diffuse reflectance absorption spectra of samples WO$_x$/x series. III) Correlation between the absorption edge energy and the size of the tungsten domain, calculated as the N$_w$ for the W supported catalysts.

Table 4
Absorption edge energies, DRS experimental results and the N$_w$ for all materials.

	E$_b$ [eV] Literature	E$_b$ [eV] experimental	N$_W$ literature	N$_W$ experimental
NaWO$_4$	4.89[b] 5.4[c]	4.91	0	0
AMT	3.23[b] 3.45[c]	3.33	4	4.1
WO$_3$	2.59[b] 2.76[d], 2.85[c]	2.69	6	5.8
W/A	4.4[a]	3.62	–	3.2
W/T	3.3[a]	3.05	–	4.9
W/S	–	2.55	–	6.2
W/Z	4.0[a]–4.3 [45]	3.58	~3.6[d]	3.5
W/AT	3.8[a]	3.20	–	4.5
W/ZT	3.4[a]	3.40	–	4.6

[a] Data from reference [31].
[b] Data from reference [37].
[c] Data from reference [41].
[d] Data from reference [42].

respectively [41]. Therefore, to validate our experimental measurements, the absorption edge energy of these reference samples was obtained from its UV–vis diffuse reflectance absorption spectra (Fig. 3-I). The following E$_b$ values for the reference compounds were obtained: 4.91 eV for NaWO$_4$, 3.35 for AMT and 2.67 for WO$_3$. These values were slightly higher (3–9%) than values reported in other referenced works. Webber [36] proposed an experimental linear fit by using the E$_b$ values of reference reagents and the concept of Mo next nearest neighbors (N$_{Mo}$) in the clusters. Scheithauer et al. also reported this kind of calculation for zirconia-supported tungsten oxide catalysts [42]. Therefore, it has been considered that the obtained values of E$_b$ for the reference compounds and their local degree of aggregation give an experimental linear fit for the W next nearest neighbors (N$_W$). The correlation was as follows: N$_W$ = 12.97–2.65*E$_b$. Then, we obtained the spectra for the WO$_x$ catalysts and we treated the data to obtain the E$_b$ for each sample. It is worth to mention at this point that this method to obtain the E$_b$ is commonly valid for pure materials and for those in

which the E_b value of the supported oxide species is very different to that of the support [43], as for A, Z, and **S** pure materials. In these, the E_b value can be obtained directly from the experimental data for the catalyst (metal-oxide/support). In the case of T, AT and ZT materials, their E_b values are close to those obtained for the W supported species. Nevertheless, the $[F(\%R)*hv]^2$ values are quite a bit higher than those seen for the supports (compare Tauc plot inset at Fig. 2 with Fig. 3-II). Therefore, we ruled out the optical contribution of the supports in all cases to obtain the E_b values listed in Table 4.

By using the linear correlation mentioned above, all values for the N_W in the different supported catalysts were obtained and plotted in Fig. 3-III. In accordance with Fig. 3-III, none of the materials have only monomeric species, because the N_W values obtained for all samples were far from the $N_W = 0$ value assigned to $NaWO_4$. The tungsten catalyst supported on S material showed the highest value of N_W, even higher than the value obtained for monoclinic crystalline WO_3. The local degree of aggregation in the synthesized materials seems not to obey the fact that AMT is preferentially ionized into $HW_6O_2^{15-}$ at impregnation conditions (pH = 3.7–5.2) [44]. It was expected that the N_W for all materials would be approximately the same, since the impregnation density of W was constant at 2.8 W atoms per nm^2. Nevertheless, the cluster size of the catalysts did not depend on this consideration. The obtained N_W values can be considered as the average sizes of the isolated tungstate monomers, medium size tungstates and some highly condensed poly-oxo tungstates [36]. Therefore, the N_w value can be taken as a measure of the tungstates average dispersion degree. The absorption edge energies found in the literature and the results obtained here for the E_b and the N_W are listed in Table 4.

3.3. Characterization of the sulfided NiW catalysts

3.3.1. DBT transformation

The catalytic activity of the supported NiW catalysts was tested in the dibenzothiophene HDS reaction at 260 °C and 490 psi of total hydrogen pressure. All catalysts were stable after passing 12 h on-stream reaction. Specific reaction rates were calculated considering steady-state conditions (Fig. 4). As shown, the highest activity was displayed by the NiW/AT catalysts followed by the NiW/ZT and NiW/A materials. In the present case, the NiW catalysts supported on T and Z presented different trends than the 3 M T reported in our previous work [24]. The NiW/Z catalyst was 20% more active than the NiW/T catalyst. It must be noted that, when the mixed oxides were used as a support, the NiW catalysts displayed the highest activities. This result is probably related to a slightly weaker interaction between the support and the W oxide phases, allowing an easy transformation into the active sulfide phases. It was also evident that intrinsic properties of the different supports can play a significant role in the catalytic activity, especially those directly related to the active phase dispersion. The NiW/**S** catalyst showed the

lowest activity despite the fact that this material exhibits suitable textural properties for this kind of process. The low catalytic activity displayed for this sample was expected, and is in good agreement with the low dispersion of W atoms detected by XRD and DRS results. The yield values were calculated for the steady state at differential regime conversion (X < 20%) (Fig. 4b). In the analysis, we took the biphenyl as a product of the DSD route and cyclohexylbenzene (CHB), bicyclohexyl (BCH), tetrahydro dibenzothiophene (THDBT) as products of the hydrogenation route according to the literature [9,13,44]. It is well known that the DBT desulfurization occurs primarily by the direct desulfurization route (DSD) over the NiW and NiMo sulfided catalysts since the effect of the Ni is to promote this pathway [46,47]. As shown in Fig. 4b, the NiW/A, NiW/Z and NiW/T displayed similar behavior with ca. 90% of DSD products. For the catalysts supported on mixed oxides (AT, ZT) a notorious increase of hydrogenation products was present up to 20% higher than for the NiW/T catalyst.

3.3.2. FTIR of adsorbed pyridine on the sulfided catalysts

FT-IR spectra of adsorbed pyridine on the NiW-x sulfided materials are shown in Fig. 5. All catalysts were recorded in the range between 1400 and 1700 cm^{-1}. As seen, all sulfided catalysts showed similar spectra. However, further analysis shows clear differences between samples. Quantitative analysis of the FT-IR spectra was done as reported in [48]. The bands at 1445 and 1538 cm^{-1} are related to characteristic antisymmetric vibrations displayed by the Lewis (L) and Brønsted (B) acid types, respectively. The band at 1489 cm^{-1} is associated with L and B sites as a contribution of the symmetrical vibrations of pyridine. The band at c.a. 1607 cm^{-1} could have contributions from the total symmetric vibration of pyridine on the L sites, from those probe molecules adsorbed via hydrogen bonding and from the anti-symmetric vibrations in the plane of pyridine B sites. The vibration observed at 1575 cm^{-1} is linked to the antisymmetric vibration in the pyridine plane on the L sites. Finally, the band around 1592 cm^{-1} is related to the symmetric vibration of pyridine on the L sites. The absence of the antisymmetric vibration and the weak symmetric vibration on the B sites is probably due to the prior degassing of the samples. This treatment leads to the removal of the −SH and −OH groups, and the signal from the B acid sites strongly decreases. Nonetheless, this is normal behavior of sulfided catalysts as reported in [49] and in [50] (and references in it). Therefore, we only analyzed the intense band at 1445 cm^{-1} and the low intensity band at 1635 cm^{-1} as directly coming from the L and B sites, respectively. The values of the area below the bands (obtained by Gaussian deconvolution) at 1635 cm^{-1} (B) and 1445 cm^{-1} (L) and the relative total area are given in Table 5.

The values in Table 5 show that the NiW/AT sulfided sample has the highest acidity (both B and L) among series. The trend in acidity observed resulted as follows NiW/AT > NiW/ZT > NiW/A > NiW/Z > NiW/T > NiW/**S**. It is well accepted that the Lewis acid sites are
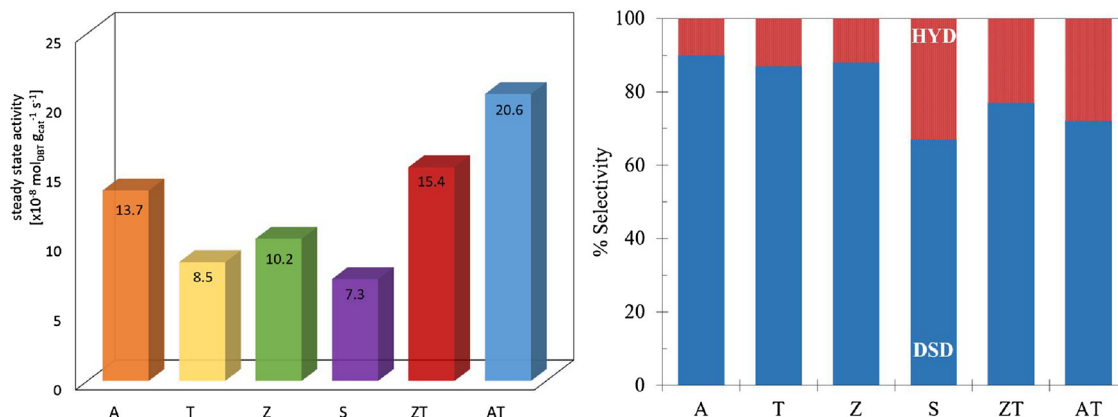

Fig. 4. a) Steady-state catalytic activity and b) selectivity for all NiW supported materials.
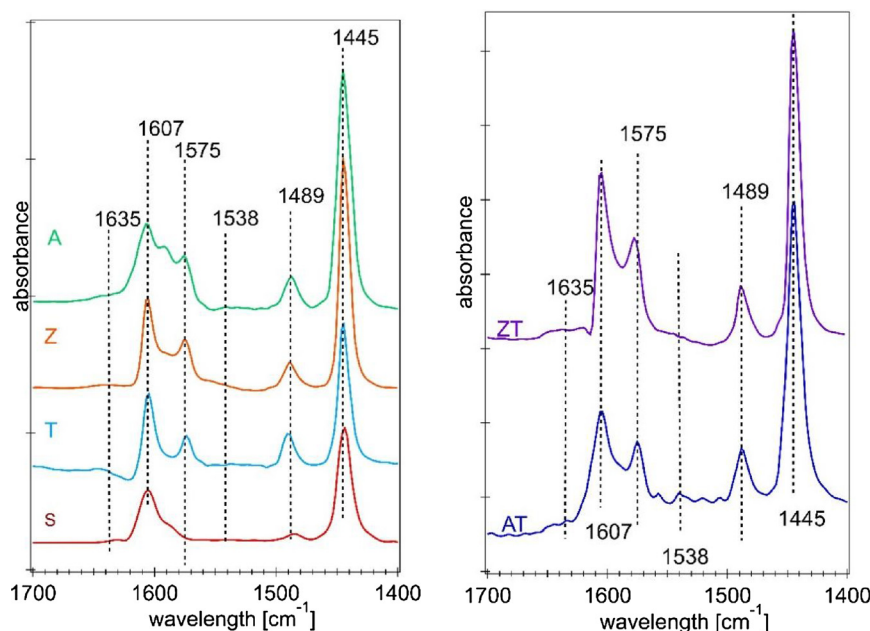
Fig. 5. IR spectra of adsorbed pyridine on the sulfided NiW/x catalyst after desorption at 393 K.

Table 5
The normalized area under the curve for bands at $1635\,cm^{-1}$ (B) and $1445\,cm^{-1}$ (L) of pyridine adsorbed on the NiW/x sulfide catalysts. The values are listed by increasing order of Lewis acid sites.

NiW/	**S**	T	A	Z	ZT	AT
Lewis sites ($1445\,cm^{-1}$)	1.5	1.6	3.0	2.3	3.4	3.9
Brønsted sites ($1635\,cm^{-1}$)	0.1	0.3	0.2	0.1	0.2	0.4
Relative total area	1.6	1.9	3.2	3.4	3.6	4.3

related to the sulfur vacancies associated with the active metals [51]. In this sense, the higher acidity of NiW/AT indicates that the sulfur vacancies are at least present in a 20% and 33% higher amount than in the NiW/ZT and NiW/A sulfided samples, respectively.

3.3.3. XPS characterization

Usually, the XPS analysis of sulfided samples is, in some particular regions, complicated to elucidate and accurate quantification of the species is difficult. In this work, we tried to keep the deconvolution process of the emission regions related to the W 4f and the Ni 2p as simple as possible. The general profile and the observed binding energies for W 4f and Ni 2p did not vary much from one support to another. Examples of the deconvolution processes are provided in Fig. 6. For the W 4f core level, the classic decomposition considers the overlapping of the characteristic doublets arising from the electrons of the W $4f_{7/2}$ and W $4f_{5/2}$ levels. Also, a small contribution related to the W $5p_{3/2}$ was typically included. In this region coexist the signal of the three possible oxidation state for W atoms: W^{6+} (oxide species), W^{5+} (oxy-sulfur species) and W^{4+} (sulfide species) (Fig. 8A). The W species observed for sulfided catalysts are shifted to low binding energies, from 35.6 and 37.8 eV for W^{6+} [52] to 33.5 and 37.7 eV for the W^{5+} [53] and to 32.2 and 34.4 eV for W^{4+} species [54]. Table 6 reports the relative concentrations for each species from the corresponding decomposition process. For Ni 2p we used the decomposition procedure previously reported [55]. As mentioned before in the case of W 4f, the Ni 2p emission region for samples NiW/A, NiW/**S**, NiW/AT and NiW/ZT was similar, although for the NiW/Z and NiW/T sulfided samples this emission was moderate, because of the low nickel loading in both catalysts (see Table 3). Thus, the decomposition process of those spectra was ruled out.
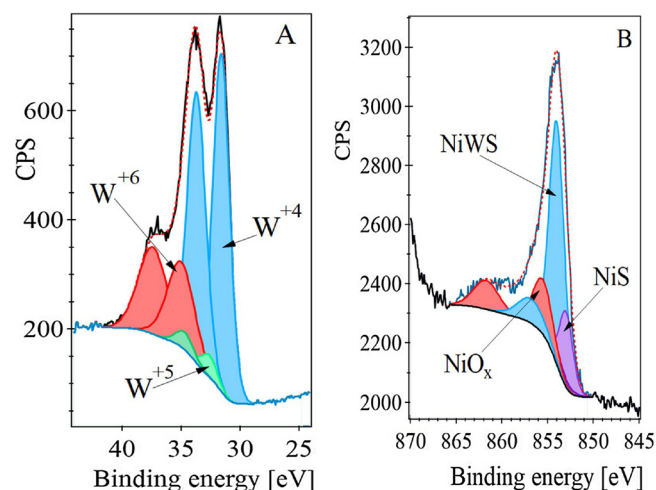

Fig. 6. Deconvolution processes for high-resolution XPS analysis of NiW/AT sulfided catalysts in the region of A) W 4f and B) Ni 2p core levels.

Table 6
Quantitative XPS analysis of NiWS/-x samples on the W 4f and Ni 2p emission regions.

NiWS/-x	WS_2 (W^{4+})	O−W−S (W^{5+})	WO_x (W^{6+})	NiO	NiWS	NiS
A	82	8	10	4	63	33
T	85	9	6	–	–	–
Z	88	8	4	–	–	–
S	89	6	5	18	68	14
AT	82	13	5	1	72	27
ZT	81	14	5	2	75	23

The spectrum obtained for the NiW/AT was chosen for a detailed description of the used methodology. Initially, the oxide signature of the Ni species was separately obtained. For the decomposition procedure, two-nickel oxide species were considered at 858.4, and 855.6 eV, and also a shake-up satellite for each of those signals to fit the spectra. In the next step, the curves described below were taken and set it into the spectrum of the NiW/AT sulfide sample to fit the spectrum. The binding energies and curves related to the NiS phase were taken from
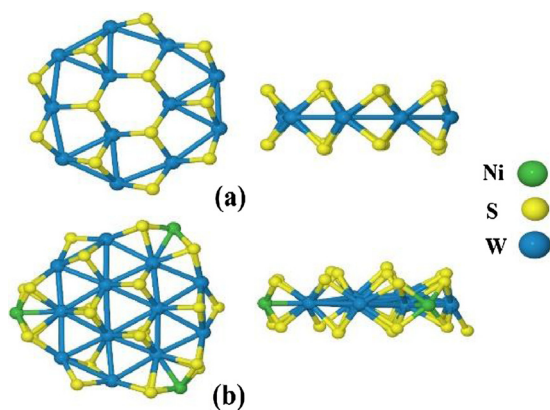
Fig. 7. Two different orientations for a) $C_1 = W_{12}S_{24}$ (WS) and b) $C_2 = Ni_3W_{12}S_{24}$ (NiWS) cluster with optimized configurations.

our previous work [55]. Thus, Ni sulfided species at 853.0 eV and two satellite peaks at 855.1 eV and 859.2 eV were used to fit the Ni 2p emission region. An example of the typical decomposition process carried out for the NiW/x sulfided samples in the Ni 2p emission region is given in Fig. 6B. As shown, a perfect fit for the Ni $2p_{3/2}$ spectral envelope was not obtained with the NiO and NiS contributions only. Therefore, a peak related to Ni in the mixed NiWS phase at 853.9 eV was added. This methodology was also used previously for NiMo [56,57] and CoMo [56,58,59] catalysts to successfully fit the sulfided XPS spectra in this region. A similar fitting process was used for all samples, and the quantifications are presented in Table 8.

3.3.4. Theoretical analysis

The supports were modeled and their configurations optimized as listed in Table 1 and mentioned in Section 2.8. The interactions of WS_2 and NiWS clusters with the supports were analyzed. First, well-defined clusters for each calculation were optimized, and they were represented as $W_{12}S_{24}$ (C_1) or $Ni_3W_{12}S_{24}$ (C_2). A view of these clusters is provided in Fig. 7 in two different orientations. Nevertheless, as it was recognized that the flat bonding via the MoS_2 basal planes appears to dominate, only this configuration was considered for optimization of the WS_2-like structure [3].

The cluster C_1 in Fig. 7a contains 12 W and 24 S atoms while the cluster C_2 in Fig. 7b has the same number of W and S atoms but with a Ni atom in each corner (3). The optimized clusters were used in the DFT calculations to obtain the E_{ads}, the number of metal-sulfur (Me−S) bonds and the average distance of the formed bonds (L[Å]), similarly to DFT adsorption energy calculations previously reported for other systems [60,61]. At the beginning of simulated interactions, the clusters were allowed to form bonds with metals (Me) or O in each support surface (Me=Al, Ti, Si, Zr). Every atom at the basal plane of the cluster was allowed to create up to two bonds with Me or O on the surface. Fig. 8 presents the optimized configurations of C_1 with the A, T, AT^{II}, and ZT^{III} supports as examples.

Firstly, all bonds created during the optimization were W-S-Me and no Mo−O−Al linkages were observed. For the C_1-A optimized configuration (Fig. 8a) the sulfur atoms interacted directly with the Al atoms forming 12 Me−S bonds. For the C_1-T optimized configuration (Fig. 8b) only part of the basal S atoms (Me−S = 4) were bonded to the support, and the C_1 cluster appeared to be tilted. A similar result was previously reported for anatase surfaces interacting with Mo_6S_n (n = 10–24) clusters [62]. When we considered the C_1-AT^{II} optimized configuration (Fig. 8c), the resulting interaction was slightly higher than the C_1-T, in this case, the Me−S bonds was equal to 7. In addition, some disorder was observed in the S atoms located on the upper plane of the C_1.

Finally, for the C1-ZT^{III} optimized configuration (Fig. 8d) the interaction was stronger than that observed for all configurations described above, In this the Me-S reached a value as high as 18 bonds. As seen, the cluster appears deformed by the interaction with the support and even a couple of S atoms were pulled out of C_1. All the images of the final C_1 and C_2 optimized configurations are provided as supplementary information in S1 and S2. The full data obtained for the E_{ads}, the Me-S bonds and the L[Å] of the bonds formed are provided in Table 7.

Data provided in Table 7 show that the C_1-ZT^{III} optimized configuration exhibited the maximum Me-S bonds formed and the highest negative E_{ads}. If we compare between ZT configurations, the ZT^{I} and ZT^{II} have almost 90% and 35% less bonds than the C_1-ZT^{III} configuration. Also, for these ZT configurations, more negative E_{ads} values were observed with an increase in the number of Me-S bonds created. It seems that, in the mixed ZT materials with the Zr atoms over the surface, the stability of the interaction with the sulfide phase is diminished in comparison with pure Z. It is worth to mention that the linear
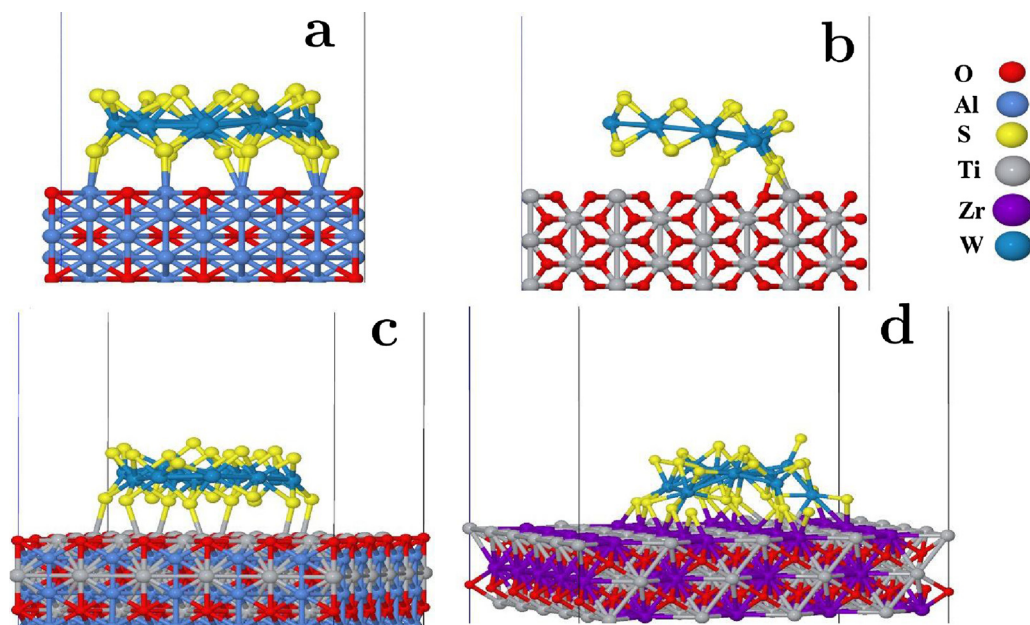

Fig. 8. Optimized configurations for the $W_{12}S_{24}$ cluster deposited on a) A, b) T, c) AT^{II} and d) ZT^{III}.

Table 7
Number of Me−S bonds, the average distance of bonding and adsorption energy (E_{ads}) for the WS_2 interactions.

Configuration with WS_2	Me−S bonding		E_{ads} [eV]
	#	L[Å]	
A	12	2.40	−17.6
AT^I	12	2.84	−16.1
AT^{II}	7	2.74	−7.4
AT^{III}	2	2.75	−7.0
T	4	2.83	−1.9
S^a	9	2.28	−15.9
S^b	11	2.25	−21.3
Z	12	2.59	−23.4
ZT^I	2	2.91	−4.1
ZT^{II}	12	2.68	−19.8
ZT^{III}	18	2.57	−36.8

Table 8
Number of Me-S bonds, average distance of bonding and adsorption energy (E_{ap}) for the NiWS interactions with the support series.

Configuration with NiWS	Me-S bonding		E_{ads} [eV]
	#	L[Å]	
A	11	2.42	−13.8
AT^I	10	2.39	−20.1
AT^{II}	8	2.68	−8.7
AT^{III}	2	2.88	−7.1
T	1	2.87	−1.7
S^a	9	2.42	−9.8
S^b	7	2.29	−14.2
Z	10	2.61	−22.5
ZT^I	5	2.88	−4.1
ZT^{II}	13	2.63	−24.8
ZT^{III}	10	2.51	−23.2

behavior described for the ZT optimized configurations was also observed for the C_1-AT configurations. Although, in this case, having the Al atoms over the surface seems to be favorable.

For the WS_2 interaction with the pure supports, we obtained the same quantity of Me−S bonds formed for the A and Z optimizations (12), while for T and S we obtained 4 and 9 Me-S bonds, respectively.

Despite the fact that the number of Me-S bonds were the same for the A and Z optimizations we did not observe an equivalent E_{ads} value for both samples. Instead, the E_{ads} value for WS_2Z optimization was −23.42 eV while for the C_1-A optimization it was −17.63 eV. As mentioned in the case of the C_1-T, the Me-S bonds were only four, with the less negative value for the E_{ads}, which means that this configuration is not favored to adsorb the WS_2 cluster. Finally, in the case of the C_1-Sa optimized configuration, the results indicated that the Sb configuration has a higher preference to adsorb the WS_2 cluster in comparison to the Sa configuration. In this C_1-Sb simulation, 11 Me−S bonds were formed, a shorter L bonding than in the C_1-Sa and it was 30% more than the E_{ads} value.

In general, the C_2-supports optimized configurations revealed that the original cluster suffers slight deformations in its overall structure (see Supporting information). We observed a collective decrease in the number of Me−S bonds and in the E_{ads} in comparison with the C_1-supports data (see Table 8). It is worth to mention that for the C_2-T simulated interaction only one single Ti−S bond was formed for anchoring the promoted cluster and the convergence criteria were reached in a tilted configuration.

4. Discussion

It is widely recognized that NiWS activity and selectivity are related to the formation, promotion, and dispersion of the NiWS active phase.

All these processes are affected by the metal support interaction. This interaction is commonly related to the sulfidation degree reached in the activation process. However, not always does a complete sulfidation lead to the highest activity as was confirmed by Breysse et al. [63] and Reinhoudt [64] et al.

In a previous work, we revised the general properties of NiW catalysts supported on A, T, Z, S as well as on AT and ZT mixed supports. Those findings revealed that each support leads to different characteristics of the WS_2 active phase, although all materials displayed the same quantity of W and Ni per square nanometer (see Table 1). The trend in catalytic activity correlated with the catalytically active W atoms located at the edge of the slabs. In the light of this finding, slab length seems to be a critical parameter. It is of paramount importance to control the final properties of a catalyst, if possible, before it is used in expensive catalytic activity tests. In this work, we approximated the W dispersion over specific supports by means of routine and inexpensive UV–vis DRS characterization.

As explained in Section 3.2.2, obtaining the E_b allowed us to calculate the number of nearest neighbors N_w. Then we searched for a possible correlation by plotting the previously reported [24] average slab length (L) as a function of these N_w values, as shown in Fig. 9.

The W catalysts prepared over the pure supports fit well with the linear correlation. However, for the NiW catalysts supported on AT and ZT mixed oxides, the L values fall out of tendency. We believe that this deviation may be related to two situations. The first one is associated with an incomplete sulfidation of the W oxide phase as observed by DRS technique where a part of the WO_x structures remain unsulfided and the slab length is shorter than expected. This may be due to a strong metal support interaction in the NiW/AT and NiW/ZT catalysts, more significant than in those supported on pure oxides. The second situation is that, when Ni was impregnated on the catalysts as the second step of the synthesis procedure (see Section 2.2), the acid solution re-dissolved some part of the WOx species weakly anchored to the support and thus provoked the re-dispersion of W. With this phenomenon, the slabs turned out to be slightly shorter than the N_w data predicted. It is necessary to remember that the DRS spectra and values related were obtained from the Ni-free catalysts. At this point, both explanations seemed possible.

To get insight into this matter, we carried out XPS characterization of the NiW sulfided catalysts. The data presented in Table 6 demonstrate that the quantification of W^{4+} species formed in the NiW/AT and NiW/ZT is more or less the same as that observed in the NiW/A catalyst. However, the quantification of W^{5+} species was notoriously more abundant in the first two catalysts, i.e., 62 and 69% higher than in the NiW/A catalyst, respectively. This fact supports the first situation, but
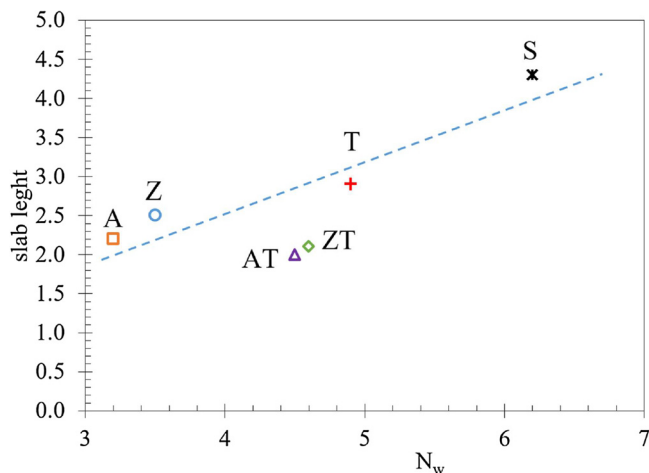
Fig. 9. Slab length from HRTEM [24] as a function of the N_w values obtained from the UV–vis DRS technique.

then, how is it possible to observe the highest catalytic activity and the best dispersion in these two catalysts?

The evidence obtained by FTIR of adsorbed NO on the sulfided catalysts allowed us to confirm that the $W^{\delta+}$ sulfided species do not correlate with the activity. Instead, the NO adsorbed on the Ni sulfur edges showed an almost linear behavior with the steady state reaction rates [24]. This statement means that the dispersion of the WS_2 slabs plays a vital role in the activity but also the relative promotion of this phase. The XPS results on Table 6 indicate that almost 72% and 75% of the Ni species are involved in the nonstoichiometric NiWS active phase for the NiW/AT and NiW/ZT, respectively. Likewise, we have now the ICP chemical analysis and the TEM statistical data. Therefore, we can use these data along with the XPS semi-quantitative analysis to obtain the % promotion of the edge tungsten atoms. The description of the entire procedure to obtain the % promotion for NiW catalysts was reported before in [55] and also used for CoMo catalysts over different supports in [57]. The % of promotion was 75, 83, and 87% for the 3 more active catalysts NiW/A, NiW/AT and NiW/ZT, respectively. These results pointed to better promotion of the active phase in catalysts prepared over AT and ZT mixed oxide even when they presented a higher content of the oxysulfide phase (WO_xS_y) and more than 20% of NiS formation. This behavior could in fact be the reason why the activity at steady state was the highest among the series; it is possible that under reaction conditions an increase of the sulfidation degree would occur. In this sense, it has been reported that Ni is typically sulfided first, if there is no chelating agent added during the synthesis procedure as in our case. However, then a part of the resulting bulk Ni sulfide is redispersed as soon as the WS_2 slabs are formed, increasing the NiWS active phase under reactions conditions [65,66].

Another fact that must be noted is the stacking degree, since it can also influence the catalytic properties [67,68]. In this sense, it is well accepted that in a sulfided catalyst at least two types of MoS-like structures are formed (Type I and Type II). Topsøe et al. proposed that type I structures are single slabs that interact strongly with the support [3]. Later studies suggested that the strong interaction mentioned before between the type I slabs and alumina support is related to the formation of Mo−O−Al linkages at the S edge ($\bar{1}$ 010) [61]. Those kinds of linkages are related to the unsulfided oxide precursors. Nevertheless, it was not our intention to simulate this process. Rather we investigated how clusters interact directly with each support bonding freely. Obviously, we are only considering the bulk structure of the supports for the current studies. Therefore, we neglected the chemical varieties of the possible Brønsted Me−OH sites, the Lewis basic Me-O-Me sites that might be present at the surface of supports [62] as well as any support sulfidation under HDS reaction conditions. Considering this, our optimization results suggest that when the studied surface models interact with a promoted or unpromoted $W_{12}S_{24}$ cluster through the basal plane, the bonding is stabilized through the S atoms. Consequently, we only observed the formation of W-S-Me bridges. Also, the calculations revealed that the interaction between the promoted cluster (C_2) and the AT configurations is more significant when only one support metal is exposed, *i.e.*, either Al or T. It should be noted that when both metals are exposed, the promoted cluster only interacts with exposed Al atoms.

In the case of the ZT calculations, the larger interaction was observed for the ZT^{II} and ZT^{III} optimized configurations. As seen in Fig S2 in the supporting information, the interaction in these cases was observed only with Zr atoms. The E_{ads} information for both configurations coincides with the E_{ads} observed for the C_2-Z optimized configuration.

Another fact that was evidenced by the theoretical calculations was that the promoted cluster tends to be bent by the interaction with the support due to a charge redistribution leading to a cluster reconfiguration and losing some crystallinity. This bending of the slabs was indeed observed experimentally in our materials. In a previous work, we presented the high-resolution transmission electron microscopy (HRTEM) images [24]. These micrograps clearly show that the slabs are slightly curved, especially in those belonging to the NiW/AT
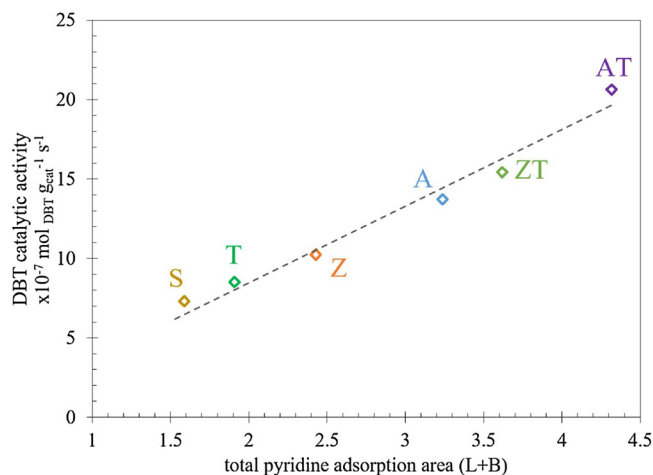

Fig. 10. HDS catalytic activity as a function of the total pyridine adsorbed for all NiW sulfided catalysts.

and NiW/ZT spent catalysts. Recently, Berhault [69] discussed this matter; he pointed out that bending possibly causes elongation of the Me–S bond length, weakening the bond strength and therefore creating defects on curved planes. This will increase the active sites formed in the inflections points of the hydrogenating character [70]. In fact, this could explain the significant improvement of selectivity for the hydrogenation route observed experimentally in these NiW/AT and NiW/ZT catalysts.

The active sites are typically quantified by probe molecules such as NO, CO or pyridine. In our previous report, we used the NO adsorption to identify the Ni^{2+} sulfide species decorating the edge or corners of the WS_2 phase, the same that correlated well with the activity of the HDS reaction of 3-methyl thiophene. In Section 3.3.2 of the present work we presented the analysis of the pyridine adsorbed on the NiW/x sulfide catalysts. The pyridine adsorption has been related primarily to sulfur vacancies which are the Lewis acid sites, and as we mentioned, to the SH- groups, that in fact could lead to another Lewis site. The results presented in Table 5 can be plotted against the activity as seen in Fig. 10. These plotted data clearly depict a linear correlation between the total pyridine adsorption area, related mainly to the active sites, and the activity on the DBT gas phase reaction.

Additionally, we would like to mention that we did not observe any direct correlation with the optical-electronic properties (E_b) of the supports and the final catalysts. While the E_b for the A, Z T, and *S* supports greatly differs, the presence of titania atoms in the mixed supports induced a shift to the typical semiconductor values for both AT and ZT supports. Several authors have proposed that the presence of Ti atoms induce higher activity due to electronic properties [35], orientations effects [71] or indirect promotion [72,73]. In fact, our results of DFT calculations showed that on Ti the orientation effects are indeed observed, as seen in Figs. S1 and S2. Nevertheless, a further examination of the mixed oxides optimized configurations (C_1 and C_2 with AT^{III} and ZT^{III}) showed that the interaction of the clusters with the supports is preferential with the Al of Zr atoms, not with Ti. In the present work, only the different configurations in question were optimized, the analysis of the electronic properties was beyond the scope of the present work. However, further DFT calculations considering the crystalline electric field and spin-orbit coupling still are in progress to describe these kinds of systems in depth.

5. Conclusions

This work shows that it is possible to approximate the active phase dispersion over specific support by carrying out routine UV–vis DRS characterization. The NiW supported on the AT and ZT mixed oxide

supports showed the highest HDS activity among the catalyst series. Also, XPS quantification of the Ni species participating in the mixed NiWS active phase pointed to a modulated interaction of this phase with AT and ZT mixed oxides; even when they presented the highest amount of the oxysulfide phase (WO_xS_y) and more than 20% of NiS formation. In fact, we propose that this could be beneficial for the catalyst since, during reaction conditions, the WO_xS_y could be fully sulfided, and the NiS be redispersed to promote the formation of new promoted WS_2 slabs. The DFT calculations showed that the optimized promoted cluster tends to be bent by the interaction with the supports due to a charge redistribution leading to a cluster reconfiguration and losing some crystallinity. This bending could derive into inflection points with hydrogenation character, which explains the experimental increase of the hydrogenation route observed. We also showed that adsorption of probe molecules such as pyridine or NO correlate well with catalytic activity tests.

Acknowledgements

Appendix A. Supplementary data

Supplementary material related to this article can be found, in the online version, at doi:https://doi.org/10.1016/j.apcatb.2018.07.059.

References

[1] A. Stanislaus, A. Marafi, M.S. Rana, Catal. Today 153 (2010) 1–68.
[2] Y. Okamoto, M. Breysse, G.M. Díaz, C. Song, Catal. Today 86 (2003) 1–3.
[3] H. Topsøe, B.S. Clausen, F.E. Massoth, Catalysis—science and technology, in: J.R. Anderson, M. Boudart (Eds.), Hydrotreating Catalysis, vol. 11, Springer-Verlag, Berlin–Heidelberg–N.Y, 1996p. 310.
[4] J.N. Díaz de León, V. Petranovskii, J.A. de los Reyes, G. Alonso-Nuñez, T.A. Zepeda, S. Fuentes, J.L. García-Fierro, Appl. Catal. A: Gen. 472 (2014) 1–10.
[5] S. Shan, P. Yuan, W. Han, G. Shi, X. Bao, J. Catal. 330 (2015) 288–301.
[6] M. Breysse, C. Geantet, P. Afanasiev, J. Blanchard, M. Vrinat, Catal. Today 130 (2008).
[7] Catal. Today 86 (2003) 1–4 all Issues.
[8] R. Huirache-Acuña, E.M. Rivera-Muñoz, B. Pawelec, M. Ostrooumov, R. Maya-Yescas, J.L. Rico, Catal. Today 220–222 (2014) 301–309.
[9] J.A. Mendoza-Nieto, F. Robles-Méndez, T.E. Klimova, Catal. Today 250 (2015) 47–59.
[10] T. Okamoto, Kubota, Catal. Today 86 (2003) 31–43.
[11] M. Breysse, P. Afanasiev, C. Geantet, M. Vrinat, Catal. Today 86 (2003) 5–16.
[12] I.D. Mora, E. Méndez, L.J. Duarte, S.A. Giraldo, Appl. Catal. A Gen. 474 (2014) 59–68.
[13] P.A. Nikulshin, P.P. Minaev, A.V. Mozhaev, K.I. Maslakov, M.S. Kulikova, A.A. Pimerzin, Appl. Catal. B: Environ. 176–177 (2015) 374–384.
[14] H. Song, J. Wang, Z. Wang, H. Song, F. Li, Z. Jin, J. Catal. 311 (2014) 257–265.
[15] H. Wu, A. Duan, Z. Zhao, D, Q, J. Li, B. Liu, G. Jiang, J. Liu, Y. Wei, X. Zhang, Fuel 130 (2014) 203–210.
[16] A.E. Cruz-Pérez, A. Guevara-Lara, J.P. Morales-Cerona, A. Alvarez-Hernandez, J.A. de los Reyes, L. Massin, C. Geantet, M. Vrinat, Catal. Today 172 (2011) 203–208.
[17] L. Chao, Z. Zhiming, H. Yongli, C. Zhenmin, Y. Weikang, Chin, J. Chem. Eng. 22 (4) (2014) 383–391.
[18] M.C. Barrera, M. Viniegra, J. Escobar, M. Vrinat, J.A. de los Reyes, F. Murrieta, J. García, Catal. Today 98 (2004) 131–139.
[19] A. Guevara-Lara, A.E. Cruz-Pérez, Z. Contreras-Valdez, J. Mogica-Betancourt, A. Alvarez-Hernández, M. Vrinat, Catal. Today 149 (2010) 288–294.
[20] J.C. Mogica-Betancourt, A. López-Benítez, J.R. Montiel-López, L. Massin, M. Aouine, M. Vrinat, G. Berhault, A. Guevara-Lara, J. Catal. 313 (2014) 9–23.
[21] J.N. Díaz de León, Appl. Catal. B: Environ. 181 (2016) 524–533.
[22] E. Kraleva, A. Spojakina, M.L. Saladino, E. Caponetti, G. Nasillo, K. Jiratova, J. Alloys Compd. 513 (2012) 310–317.
[23] J. Escobar, J.A. De Los Reyes, C.A. Ulín, M.C. Barrera, Mat. Chem. Phys. 143 (2013) 213–222.
[24] J.N. Díaz de León, L.A. Zavala-Sánchez, V.A. Suárez-Toriello, G. Alonso-Núñez, T.A. Zepeda, R.I. Yocupicio, J.A. de los Reyes, S. Fuentes, Appl. Catal. B Environ. 213 (2017) 167–176.
[25] M. Ramos, G. Berhault, D.A. Ferrer, B. Torres, R.R. Chianelli, Catal. Sci. Technol. 2 (2012) 164–178.
[26] D.G. Barton, M. Shtein, R.D. Wilson, S.L. Soled, E. Iglesia, J. Phys. Chem. B 103 (1999) 630–640.
[27] P. Giannozzi, S. Baroni, N. Bonini, M. Calandra, R. Car, C. Cavazzoni, D. Ceresoli, G.L. Chiarotti, M. Cococcioni, I. Dabo, A. Dal Corso, S. de Gironcoli, S. Fabris, G. Fratesi, R. Gebauer, U. Gerstmann, C. Gougoussis, A. Kokalj, M. Lazzeri, L. Martin-Samos, N. Marzari, F. Mauri, R. Mazzarello, S. Paolini, A. Pasquarello, L. Paulatto, C. Sbraccia, S. Scandolo, G. Sclauzero, A.P. Seitsonen, A. Smogunov, P. Umari, R.M. Wentzcovitch, J. Phys. Condens. Matter 21 (2009) 1–19 395502.
[28] J. Perdew, K. Burke, M. Ernzerhof, Phys. Rev. Lett. 77 (1996) 3865–3868.
[29] The pseudopotentials used in this work were taken from quantum-espresso web page. http://www.quantum-espresso.org.
[30] J.A. Mendoza-Nieto, I. Puente-Lee, C. Salcedo-Luna, T. Klimova, Fuel 100 (2012) 100–109.
[31] A. Gutierrez, J. Ramirez, G. Busca, Catal. Lett. 56 (1998) 29–33.
[32] M.A. Larrubia, G. Busca, Mater. Chem. Phys. 72 (3) (2001) 337–346.
[33] R. Palcheva, L. Dimitrov, G. Tyuliev, A. Spojakina, K. Jiratova, Appl. Surf. Science 265 (2013) 309–316.
[34] T.A. Zepeda, J.L.G. Fierro, B. Pawelec, R. Nava, T. Klimova, G.A. Fuentes, T. Halachev, Chem. Mater. 17 (2005) 4062–4073.
[35] J. Ramirez, G. Macias, L. Cedeño, A. Gutierrez-Alejandre, R. Cuevas, P. Castillo, Catal. Today 98 (2004) 19–30.
[36] R.S. Webber, J. Catal. 151 (1995) 470–474.
[37] D.G. Barton, M. Shtein, R.D. Wilson, S.L. Soled, E. Iglesia, J. Phys. Chem. B 103 (1999) 630–640.
[38] E.O. Filatova, A.S. Konashuk, J. Phys. Chem. C 119 (2015) 20755–20761.
[39] S. Toyoda, T. Shinohara, H. Kumigashira, M. Oshima, Y. Kato, Appl. Phys. Lett. 101 (2012) 231607–231610.
[40] D. Zuo, D. Li, H. Nie, Y. Shi, M. Lacroix, M. Vrinat, J. Mol. Catal. A Chem. 211 (2004) 179–189.
[41] M. Valigi, D. Gazzoli, I. Pettiti, G. Mattei, S. Colonna, S. De Rossi, G. Ferraris, Appl. Catal. A Gen. 231 (2002) 159–172.
[42] M. Scheithauer, R.K. Grasselli, H. Knozinger, Langmuir 14 (1998) 3019–3029.
[43] X. Gao, I.E. Wachs, J. Phys. Chem. B 104 (2000) 1261–1268.
[44] J.N. Díaz de León, M. Picquart, M. Villarroel, M. Vrinat, F.J. Gil Llambías, F. Murrieta, J.A. de, los Reyes, J. Mol. Catal. A Chem. 323 (2010) 1–6.
[45] I.E. Wachs, T. Kim, E.I. Ross, Catal. Tod. 116 (2006) 162–168.
[46] Q. Gao, T.N.K. Ofosu, S.G. Ma, V.G. Komvokis, C.T. Williams, K. Segawa, Catal. Today 164 (2011) 538–543.
[47] J.N. Díaz de León, T.A. Zepeda, G. Alonso-Nuñez, D.H. Galván, B. Pawelec, S. Fuentes, J. Catal. 321 (2015) 51–61.
[48] T.A. Zepeda, B. Pawelec, J.L.G. Fierro, T. Halachev, J. Catal. 242 (2006) 254–269.
[49] N.Y. Topsøe, H. Topsøe, F.E. Massoth, J. Catal. 119 (1989) 252–255.
[50] M. Breysse, G. Berhault, S. Kasztelan, M. Lacroix, F. Maugé, G. Perot, Catal. Today 66 (2001) 15–22.
[51] K. Tanabe, M. Misono, Y. Ono, H. Hattori, Stud. Surf. Sci. Catal. 51 (1989) Elsevier.
[52] E. Rodriguez, A. Jimenez, D. Eliche, Fuel 87 (2008) 1195–1206.
[53] L. Coulier, G. Kishan, J.A.R. van Veen, J.W. Niemantsverdriet, J. Phys. Chem. B 106 (2002) 5897–5906.
[54] H.R. Reinhoudt, E. Crezee, A.D. van Langeveld, P.J. Kooyman, J.A.R. van Veen, J.A. Moulijn, J. Catal. 196 (2000) 315–329.
[55] J.N. Díaz de León, M. Picquart, L. Massin, M. Vrinat, J.A. de los Reyes, J. Mol. Catal. A 363–364 (2012) 311–321.
[56] A.F. Lamic, A. Daudin, S. Brunet, C. Legens, C. Bouchy, E. Devers, Appl. Catal. A Gen. 344 (2008) 198–204.
[57] T.K.T. Ninh, L. Massin, D. Laurenti, M. Vrinat, Appl. Catal. A Gen. 407 (2011) 29–39.
[58] B. Guichard, M. Roy-Auberger, E. Devers, C. Legens, P. Raybaud, Catal. Today 130 (2008) 97–108.
[59] T.K.T. Ninh, D. Laurenti, E. Leclerc, M. Vrinat, Appl. Catal. A Gen. 487 (2014) 210–218.
[60] M. Yokoyama, K. Nakada, A. Ishii, Comput. Mater. Sci. 82 (2014) 231–236.
[61] J. Shah, S. Kansara, S.K. Gupta, Y. Sonvane, Phys. Lett. A 381–36 (2017) 3084–3088.
[62] C. Arrouvel, M. Breyse, H. Toulhoat, P. Raybaud, J. Catal. 232 (2005) 161–178.
[63] M. Breysse, M. Cattenot, T. Decamp, R. Frety, C. Gachet, M. Lacroix, C. Leclerq, L. de Mourques, J.L. Portefaix, M. Vrinat, M. Houari, J. Grimblot, S. Kasztelan, J.P. Bonnelle, Housni S, J. Bachelier, J.C. Duchet, Catal. Today 4 (1988) 39–55.
[64] H.R. Reinhoudt, A.D. van Langeveld, R. Mariscal, V.H.J. de Beer, J.A.R. van Veen, S.T. Sie, J.A. Moulijn, Stud. Surf. Sci. Catal. 106 (1997) 263–271.
[65] H.R. Reinhoudt, Y. van der Meer, A.M. van der Kraan, A.D. van Langeveld, J.A. Moulijn, Fuel. Proc. Tecnol. 61 (1999) 43–54.
[66] M.J. Vissenberg, Y. van der Meer, E.J.M. Hensen, V.G.J. de Beer, A.M. van der Kraan, R.A. van Santen, J.A.R. van Veen, J. Catal. 198 (2001) 151–163.
[67] B. Hinnemann, J.K. Norkov, H. Topsoe, J. Phys. Chem. B 109 (2005) 2245–2253.
[68] G.A. Gonzales, M. Alvarado, M. Ramos, G. Berhaul, R.R. Chianelli, Comput. Mater. Sci. 123 (2016) 93–105.
[69] G. Berhault, New Materials for Catalytic Applications, Elsevier, 2016 Ch. 10, 336.
[70] Y. Iwata, Y. Araki, K. Honna, Y. Miki, K. Sato, H. Shimada, Catal. Today 65 (2001) 335–341.
[71] Y. Araki, K. Honna, H. Shimada, J. Catal. 207 (2002) 361–370.
[72] L. Coulier, J.A.R. van Veen, J.W. Niemantsverdriet, Catal. Lett. 79 (2002) 149–155.
[73] C. Arrouvel, H. Toulhoat, M. Breysse, P. Raybaud, J. Catal. 226 (2004) 260–272.